

Polarization-discrimination technique to maximize the lidar signal-to-noise ratio for daylight operations

Yasser Y. Hassebo, Barry Gross, Min Oo, Fred Moshary, and Samir Ahmed

The impact and potential of a polarization-selection technique to reduce the sky background signal for linearly polarized monostatic elastic backscatter lidar measurements are examined. Taking advantage of naturally occurring polarization properties in scattered skylight, we devised a polarization-discrimination technique in which both the lidar transmitter and the receiver track and minimize detected sky background noise while maintaining maximum lidar signal throughput. Lidar elastic backscatter measurements, carried out continuously during daylight hours at 532 nm, show as much as a factor of $\sqrt{10}$ improvement in the signal-to-noise ratio (SNR) over conventional unpolarized schemes. For vertically pointing lidars, the largest improvements are limited to the early morning and late afternoon hours, while for lidars scanning azimuthally and in elevation at angles other than vertical, significant improvements are achievable over more extended time periods with the specific times and improvement factors depending on the specific angle between the lidar and the solar axes. The resulting diurnal variations in SNR improvement sometimes show an asymmetry with the solar angle that analysis indicates can be attributed to changes in observed relative humidity that modifies the underlying aerosol microphysics and observed optical depth. © 2006 Optical Society of America

OCIS codes: 280.3640, 280.0280, 280.1100, 010.3640.

1. Introduction

We describe a technique that is designed to improve the operation of conventional elastic backscatter lidars in which the transmitted signal is generally linearly polarized. The technique requires the use of a polarization-sensitive receiver. Polarization-selective lidar systems have, in the past, been used primarily for separating and analyzing the polarization of lidar returns, for a variety of purposes, including the examination of multiple-scattering effects and for differentiating between different atmospheric scatterers and aerosols.¹⁻⁹ In the approach described here, the polarized nature of the sky background light is used to devise a polarization-selective scheme to reduce the sky background power detected in a lidar. This leads to improved signal-to-noise ratios (SNRs)

and attainable lidar ranges, which are important considerations in daylight lidar operation.^{10,11}

The approach discussed here is based on the fact that most of the energy in linearly polarized elastically backscattered lidar signals retains the transmitted polarization,^{1,6,9} while the received sky background power (P_b) observed by the lidar receiver shows polarization characteristics that depend on both the scattering angle θ_{sc} between the direction of the lidar and the direct sunlight and the orientation of the detector polarization relative to the scattering plane. In particular, the sky background signal is minimized in the plane perpendicular to the scattering plane, while the difference between the in-plane component and the perpendicular components (i.e., as degree of polarization) depends solely on the scattering angle. For a vertically pointing lidar, the scattering angle θ_{sc} is the same as the solar zenith angle θ_s in Fig. 1. The degree of polarization of the sky background signal observed by the lidar is largest for solar zenith angles near $\theta_s \approx 90^\circ$ and smallest at solar noon. The essence of the proposed approach is therefore, at any time, to first determine the parallel component of P_b with a polarizing analyzer on the receiver, thus minimizing the detected P_b , and then orienting the polarization of the outgoing lidar signal so that the polarization of the received lidar backscatter signal is aligned with the receiver polarizing an-

The authors are with the Optical Remote Sensing Laboratory, Department of Electrical Engineering, The City College of the City University of New York, Convent Avenue and 140 Street, New York, New York 10031. S. Ahmed's e-mail address is ahmed@cuny.cuny.edu.

Received 4 November 2005; revised 20 April 2006; accepted 26 April 2006; posted 27 April 2006 (Doc. ID 65757).

0003-6935/06/225521-11\$15.00/0

© 2006 Optical Society of America

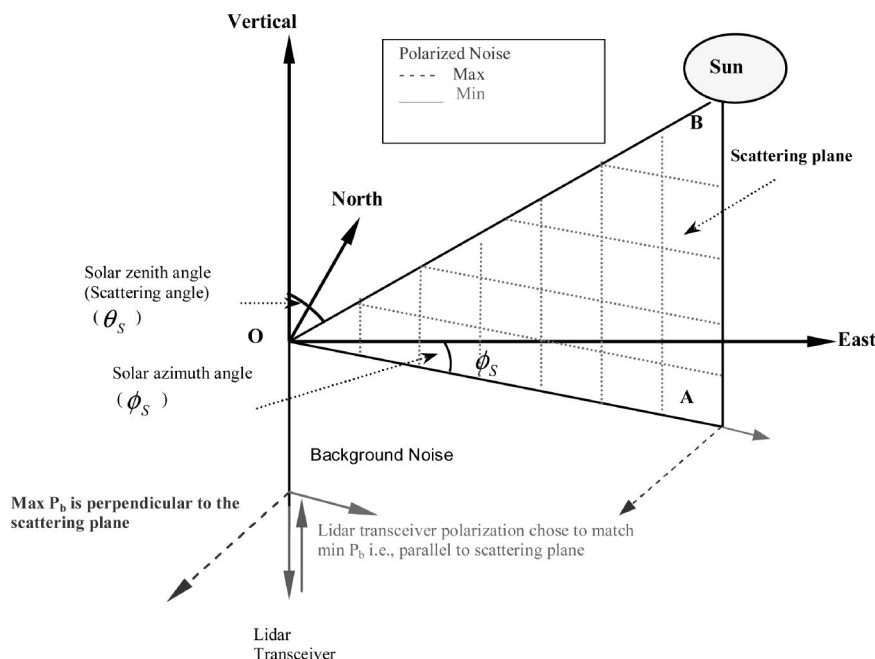


Fig. 1. Sky background suppression geometry for a vertical pointing lidar: θ_s is the solar zenith angle (equal to the scattering angle for this geometry), ϕ_s is the solar azimuth angle and OAB is the solar scattering plane.

alyzer. This ensures the unhindered passage of the primary lidar backscatter returns, while at the same time minimizing the received sky background P_b , and thus maximizing both the SNR and the attainable lidar ranges.

The experimental approach and system geometry to implement the polarization discrimination scheme are described in Section 2. Section 3 presents the results of the elastic lidar backscatter measurements for a vertically pointing lidar at 532 nm taken on a clear day in the New York City urban atmosphere, which examine the range of application of the technique. In particular, the diurnal variations in P_b as functions of different solar angles are given, and the SNR improvement is shown to be consistent with the results predicted from the measured degree of linear polarization, with maximum improvement restricted to the early morning and late afternoon. Section 4 examines the situations in which asymmetric diurnal variations in sky P_b are observed, and demonstrates the possibility that an increase in relative humidity (RH), consistent with measured increases in measured precipitable water vapor (PWV) and aerosol optical depth (AOD), may account for the asymmetry.

Analysis of the overall results is presented in Section 5, where the SNR improvement factor is compared with single-scattering radiative transfer theory. Possible modifications due to multiple scattering are also explored. In Section 6, the diurnal variation of the polarization rotation angle is compared to the theoretical result and an approach for automation of the technique based on theory is discussed. In addition, the potential impact of the method on lidars scanning azimuthally and in elevation at angles other than vertical is examined and shown to have a much wider range of effective operational periods during the day

compared to vertical lidars. The conclusions and summary are presented in Section 7.

2. Experimental Approach and System Geometry

The City University of New York (CUNY) has developed two ground-based lidar systems, one mobile and one stationary, that operate at multiple wavelengths for monostatic elastic backscatter retrievals of aerosol and cloud characteristics and profiles. Lidar measurements are performed at the Remote Sensing Laboratory of the City College of New York (CCNY). The lidar systems are designed to monitor enhanced aerosol events as they traverse the eastern coast of the United States, and form part of the National Oceanic and Atmospheric Administration's (NOAA's) Cooperative Remote Sensing Center (CREST) Regional East Atmospheric Lidar Mesonet (REALM) lidar network. The lidar measurements reported here were carried out with the mobile elastic monostatic biaxial backscatter lidar system at the CCNY site (longitude 73.94 W, latitude 40.83 N), at a 532 nm wavelength. The lidar transmitter and the receiver subsystems are detailed in Table 1. The lidar return from the receiver telescope is detected by a photomultiplier (PMT R11527P) with a 1 nm bandwidth optical filter (532F02-25 Andover), centered at the 532 nm wavelength. For extended ranges, data are acquired in the photon counting (PC) mode, typically averaging 600 pulses over a 1 min interval and using a Licel 40-160 transient recorder with a 40 MHz sampling rate for analog-to-digital conversion and a 250 MHz photon counting sampling interval. Figure 2 shows the arrangement used to implement the polarization-tracking scheme. To select the polarization of light entering the detector, a polarizing beam splitter is located in front of the collimating lens that is used in conjunction with a narrowband filter (al-

Table 1. Lidar System Specifications

Transmitter		Receiver	
Laser	Q-switched Nd:YAG Telescope continuum surelite 11-10	CM_1400 Schmidt	
		Aperture	Cassegrain telescope 35.56 mm
Wavelength	1064, 532, 355 nm	Focal length	3910 mm
Energy-pulse	650 mJ at 1064 nm	Detectors	Hamamatsu
	300 mJ at 532 nm	532 nm	PMT: R11527 P
	100 mJ at 355 nm	355 nm	PMT: R758-10
		1064 nm	Avalanche photodiode
Pulse duration	7 ns at 1064 nm	Data acquisition	LICEL transient recorder 40-160
Repetition rate	10 Hz	Photon counting	LICEL transient recorder 40-160
Harmonic generation	Surelite double Surelite third harmonic		

ternatively, dichroic material polarizers were also used). This polarizing beam splitter (analyzer) is then rotated to minimize the detected sky background P_b . Cross-polarized extinction ratios on the receiver analyzer were approximately 10^{-4} . On the transmission side, a half-wave plate at the output of the polarized laser output is then used to rotate the polarization of

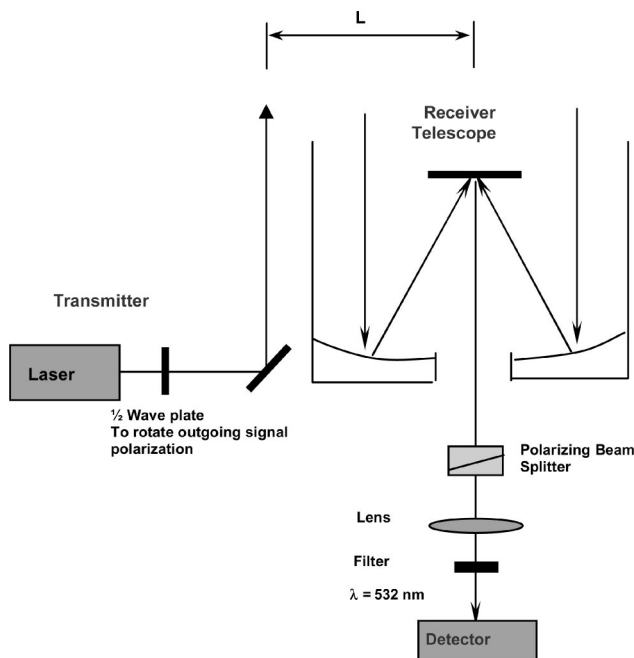


Fig. 2. Schematic of the polarization experiment setup for elastic biaxial monostatic lidar (mobile lidar system).

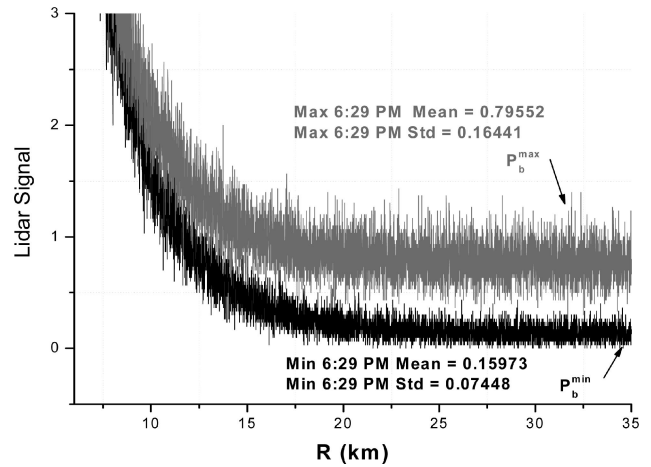


Fig. 3. Comparison of max P_b versus min P_b lidar signals at 6:29 p.m. on 7 October 2004.

the outgoing lidar beam so as to align the polarization of the backscattered lidar signal with the receiver polarizing analyzer, and hence maximize its throughput (i.e., at the minimum P_b setting). This procedure was repeated for all the measurements, with appropriate adjustments being made in the receiver polarization analyzer alignment and a corresponding tracking alignment in the transmitted beam polarizations to adjust for different solar angles at different times of the day, and hence minimize the detected P_b and maximize the lidar SNR.

3. Results

A. Lidar Data

Figure 3 shows an example of experimental results (6:29 p.m. 7 October 2004) obtained for different polarization alignments. All the times given are in Eastern Standard Time. The detected lidar signal is the sum of atmospheric backscatter of the laser pulse and the detected background light. The upper trace corresponds to the receiver polarization analyzer oriented to minimize P_b and the lidar transmitter polarization oriented to maximize the detected backscattered lidar signal while the lower trace is the result when orthogonal orientations of both receiver analyzer and lidar polarization are used, minimizing the sky background component in the return signal. Similar measurements were made at noon and 3:00 p.m. on the same day. Figure 4 shows the resulting return signals in the far zone where the sky background signal is the dominant component (20–30 km range) for these times and for both orthogonal polarizations. The relative impact on the sky background signal P_b of the polarization-discrimination scheme is seen to be largest at 6:29 p.m., when the lidar solar angle is large (89°), while at noon it is minimal. The detected signal for maximum P_b is much noisier than the detected signal with minimum P_b , except in the noon measurement. This is consistent with the shot-noise limit applicable to photomultiplier tubes (PMTs), where the detected noise amplitude ΔP

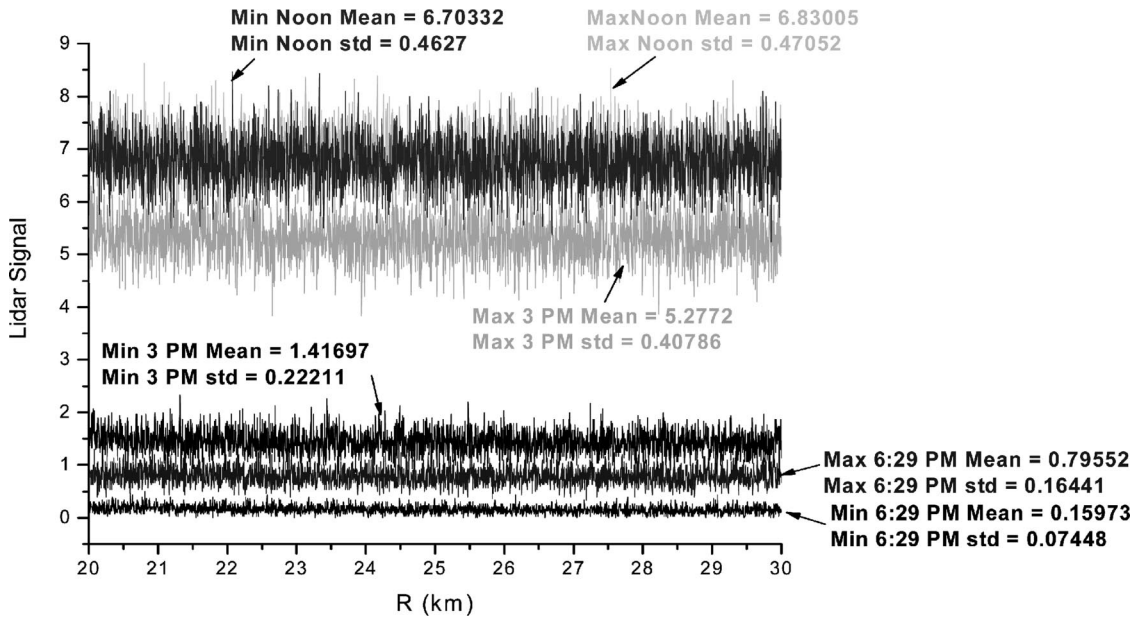


Fig. 4. Comparison of experimental return signals at 6:29 p.m., 3 p.m. and noon on 7 October 2004, range of 20–30 km both orthogonal cases are shown.

(standard deviation) is proportional to the square root of the mean detected background signal $\langle P \rangle$ (i.e., $\Delta P \propto \sqrt{\langle P \rangle}$), where P is the detector output whose mean value is proportional to P_b . This relation is most conveniently expressed in terms of the ratios of the detected signals at the orthogonal polarization states $R = P_b^{\max}/P_b^{\min}$, in which the shot-noise condition is now $\Delta R = \sqrt{R}$. This relation has been verified in our experiments and the results are summarized in Table 2.

In assessing the extent to which the polarization-discrimination detection scheme can improve the SNR and the operating range, we compare the detected SNR with a polarizer, to that which would be obtained if no polarization filtering was used. When shot noise from background light is large compared to that from the lidar signal backscatter, the SNR improvement can be expressed in terms of an SNR improvement factor (G_{imp}) expressed in terms of maximum and minimum P_b measurements (P_b^{\max} , P_b^{\min}) as

$$G_{\text{imp}} = \frac{\text{SNR}_{\text{Max}}}{\text{SNR}_{\text{Unpol}}} = \sqrt{\left(\frac{P_b^{\min} + P_b^{\max}}{P_b^{\min}}\right)} = \sqrt{1 + \left(\frac{P_b^{\max}}{P_b^{\min}}\right)}. \quad (1)$$

To examine how the decreased P_b translates into a

SNR improvement, Fig. 5 shows the range-dependent SNR obtained for both maximum and minimum noise polarization orientations for a representative lidar measurement. The results show that for SNR = 10, the range improvement resulting from polarization discrimination resulted in an increase in the lidar operating range from 9.38 to 12.5 km (a 34% improvement). Alternatively, for a given lidar range, say 9 km, the SNR improvement was 250%. Another useful way of looking at the effect of SNR improvement is to note that the SNR improves as the square root of the detector's averaging time. Thus a 250% improvement in SNR is equivalent to reducing the required averaging time by a factor of $(1/2.5)^2$.

B. Signal-to-Noise Ratio Improvement with Respect to the Solar Zenith Angle

The SNR improvement factor (G_{imp}) is plotted as a function of the local time, Fig. 6(a), and the solar zenith angle, Fig. 6(b). Since the solar zenith angle retraces itself as the Sun passes through solar noon, it would be expected that the improvement factor (G_{imp}) would be symmetric before and after solar noon and depend solely on the solar zenith angle. This symmetry is observed in Figs. 6(a) and 6(b) for measurements made on 19 February 2005 and is supported by the relatively small changes in AOD values

Table 2. Comparison of Experimental Results to Verify Shot-Noise Operation ($\Delta R = \sqrt{R}$)

Time	$\langle P_{\min} \rangle$	ΔP_{\min}	$\langle P_{\max} \rangle$	ΔP_{\min}	$R = \frac{\langle P_{\max} \rangle}{\langle P_{\min} \rangle}$	$\Delta R = \frac{\Delta P_{\max}}{\Delta P_{\min}}$	\sqrt{R}
Noon	6.7	0.46	6.83	0.46	1.2	1.019	1.09
3:00 p.m.	1.41	0.22	5.27	0.22	3.72	1.82	1.9
6:29 p.m.	0.159	0.074	0.795	0.074	5.2	2.2	2.2

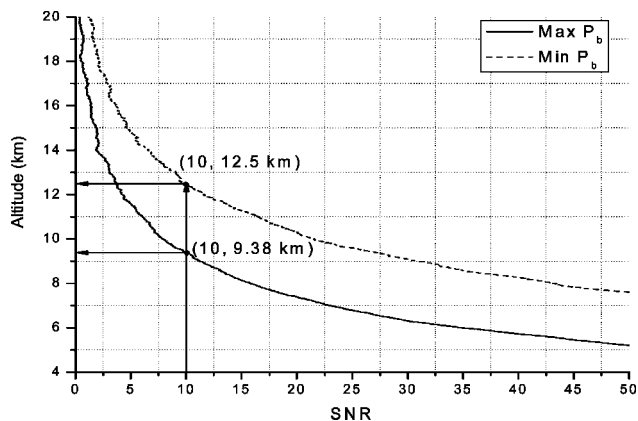


Fig. 5. Experimental range-dependent SNR for maximum and minimum polarization orientations.

obtained from a collocated shadow-band radiometer (morning $\tau = 0.08$, afternoon $\tau = 0.11$).

4. Effect of Variable Precipitable Water Vapor on the Signal-to-Noise Ratio

Symmetry was, however, not always observed in our experimental results. Figure 7 shows G_{imp} plotted as a function of the solar zenith angle for 23 February 2005. Small asymmetries were observed. These appear to be related to changes in humidity, which can modify the scattering properties and lead to enhanced multiple-scattering effects. The results are supported by the variation in PWV shown in Fig. 8,

obtained from the CCNY global positioning system (GPS) measurements that were processed by the NOAA Forecast Systems Laboratory¹² (FSL) for both days. On 23 February, the aerosol optical depth measurements from the shadow-band radiometer show larger proportional changes (morning $\tau = 0.16$, afternoon $\tau = 0.09$) than those of 19 February, which are consistent with the asymmetry in the PWV, with higher optical depths corresponding to high PWV (and RH %) conditions.

5. Discussion and Analysis

To qualitatively compare the extent of P_b polarization observed in our experiments with theoretical estimates, we use a single-scattering model of the atmosphere, justified by the relatively small optical depths measured by sky radiometry during the experiments. In this limit, P_b is simply proportional to the diffuse transmission, T , of sunlight through the atmosphere, which takes the form:

$$T_i(\mu; \mu_o) = \frac{\tilde{\omega}}{4(\mu - \mu_o)} P_i^{\text{eff}}(e^{-\tau/\mu} - e^{-\tau/\mu_o}), \quad (2)$$

where $i = 1, 2$ for parallel (in-plane) and perpendicular (out-of-plane) polarization, respectively, μ_o , μ are direction cosines of the solar and viewing angles, τ is the total optical depth, and $\tilde{\omega}$ is the single-scattering albedo. P_1^{eff} and P_2^{eff} are the effective phase functions for the parallel and perpendicular components corresponding to the minimum P_b and maxi-

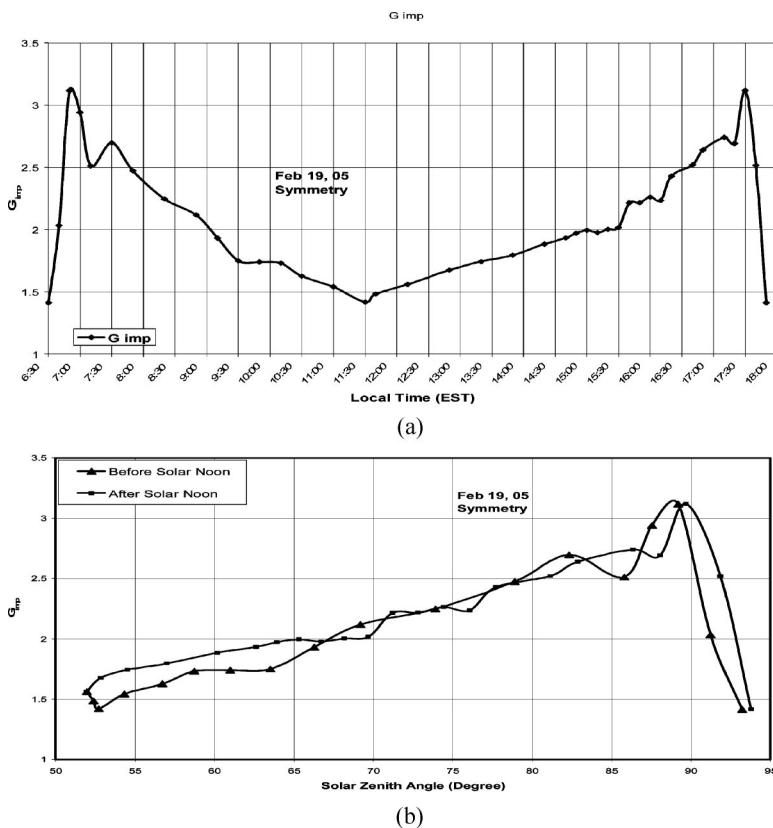


Fig. 6. (a) G_{imp} in detection wavelength of 532 nm versus local time on 19 February 2005. (b) G_{imp} in detection wavelength of 532 nm versus solar zenith angle on 19 February 2005.

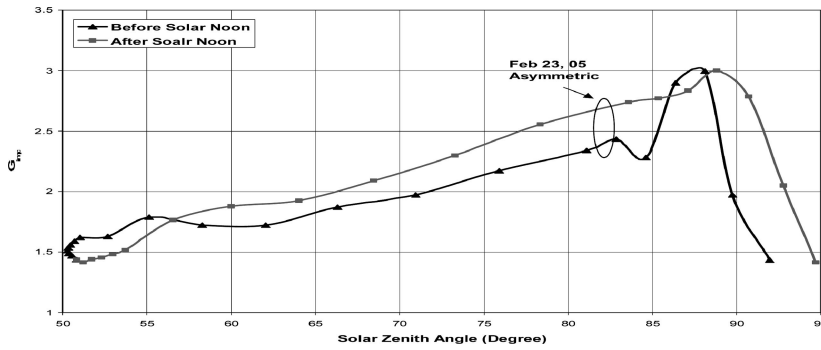


Fig. 7. G_{imp} in detection wavelength of 532 nm versus solar zenith angle on 23 February 2005.

mum P_b . For a two-component atmosphere consisting of a mixture of aerosol and molecules where τ_{mol} and τ_{aer} are the optical depths for molecular and aerosol components. The effective phase functions are then a weighted combination given by

$$P_i^{\text{eff}} = \frac{\tau_{\text{mol}} P_i^{\text{mol}} + \tau_{\text{aer}} P_i^{\text{aer}}}{\tau_{\text{mol}} + \tau_{\text{aer}}}, \quad (3)$$

where the total phase functions for the molecular component can be written as

$$P_{\text{Tot}}^{\text{mol}} = \frac{3}{4} [1 + \cos^2(\theta_{\text{sc}})]. \quad (4)$$

The molecular optical thickness is obtained from the following empirical formula:

$$\tau_{\text{mol}} = C_o \left(\frac{\lambda}{\lambda_o} \right)^{-4} \left[1 + C_1 \left(\frac{\lambda}{\lambda_o} \right)^{-2} + C_2 \left(\frac{\lambda}{\lambda_o} \right)^{-4} \right], \quad (5)$$

where the parameter values are $C_o = 0.09364$, $C_1 = 0.0374$, $C_2 = 0.00142$, and $\lambda_o = 550$ nm.¹³ The equivalent effective phase functions for the aerosol components depend on the normalized particulate distribution function used, and are approximated (assuming spherical particles) by

$$P_i^{\text{aer}} = S_i(\theta_{\text{sc}}) \left(\frac{4}{q^2 Q_e} \right), \quad (6)$$

$$S_i(\theta_{\text{sc}}) = \int S_i^{\text{norm}}(r, \theta_{\text{sc}}) \bar{n}(r) dr. \quad (7)$$

Here, S_i is the scattering function for each polarization, Q_e is the Mie extinction efficiency, which is a function of the normalized size parameter $q = 2\pi a/\lambda$ where a is the particle radius and λ is the wavelength, $\bar{n}(r)$ is the particle size distribution, and S_i^{norm} is the normalized single-particle-scattering function (for a given polarization).^{14–16} We obtain from Eq. (2), the ratio of the maximum noise P_b^{max} to the minimum noise P_b^{min} as

$$\frac{P_b^{\text{max}}}{P_b^{\text{min}}(\theta_{\text{sc}})} = \frac{T^\perp(\mu; \mu_o)}{T^\parallel(\mu; \mu_o)} = \frac{P_2^{\text{eff}}}{P_1^{\text{eff}}}, \quad (8)$$

from which, the SNR improvement function G_{imp} can be theoretically estimated using Eq. (1). To evaluate this expression, the optical depth of both the molecular and the aerosol components as well as the angular dependence of the phase functions should be known.

A. Symmetric Data Set

The conditions on 19 February 2005 were quite clear and dry, with rather small optical thickness. We therefore used a fine-mode-dominated aerosol particle size distribution representative of “clear” conditions together with the sky radiometry measured optical thickness $\tau_{\text{aer}} = 0.1$. The use of the fine-mode

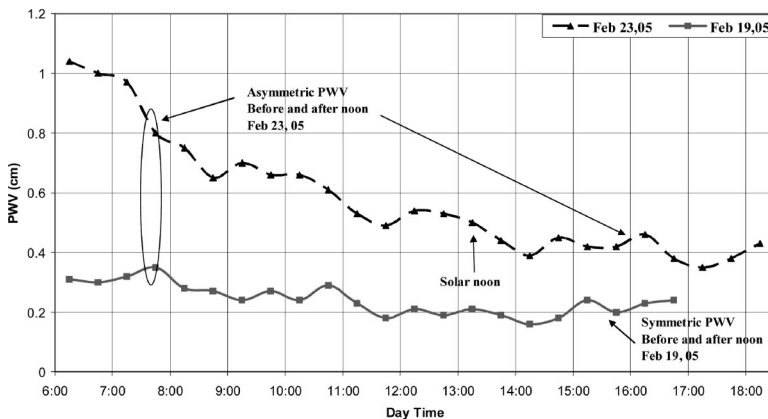


Fig. 8. PWV (cm) loading versus local time on 19 February 2005 and 23 February 2005.

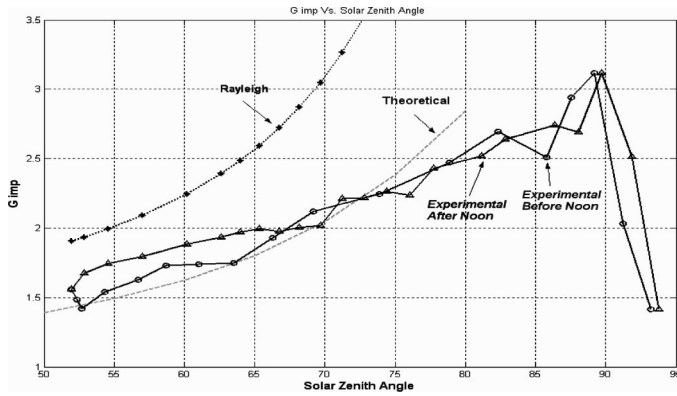


Fig. 9. Theoretical model agrees with experimental measurements, 19 February 2005. Rayleigh scattering alone is also shown.

aerosol was justified by a fairly sharp decrease in aerosol optical depth as a function of wavelength resulting in an angstrom coefficient $\gamma = -1.6$. The comparisons between measurements and theoretical results for a single-scattering model are given in Fig. 9. This shows G_{imp} as a function of the solar zenith angle for a day where PWV variation between morning and afternoon was not significant (recall $\theta_{\text{sc}} = \theta_s$ for a vertically pointing lidar). Reasonably good agreement is seen between the theory and observations. Very similar results were obtained on other low PWV variation days (1, 2 February 2005). For comparison, the G_{imp} expected for a completely clear sky due to Rayleigh scattering alone is also shown, where:

$$G_{\text{imp}}^{\text{Ray}} = \sqrt{1 + s^2(\theta_{\text{sc}})}, \quad (9)$$

which is obtained by combining Eqs. (4) and (8). It is clear that G_{imp} is significantly affected by the impact of even fairly low levels of aerosols.

B. Asymmetric Data Set

The asymmetric data of 23 September 2005 can be explained by considering the effects of changes in aerosol particle sizes and refractive index in a moist environment (high RH), because water in the air condenses onto the aerosol. The growth in particle size due to the condensation of water vapor can be described as¹⁶

$$r(a_w) = r_o \left[1 + \rho \frac{m_w(a_w)}{m_o} \right]^{1/3}, \quad (10)$$

where the water activity a_w of a soluble aerosol at radius r (μm) can be expressed as

$$a_w = \text{RH} \exp \left[\frac{2\sigma V_w}{R_w T} \frac{1}{r(a_w)} \right], \quad (11)$$

where r_o is the dry particle radius, ρ is the particle density relative to that of water, $m_w(a_w)$ is the mass of condensed water, m_o is the dry particle mass, RH is the relative humidity, σ is the surface tension on the

wet surface, V_w is the specific volume of water, R_w is the gas constant for water vapor, and T is the absolute temperature (K). The refractive index for the wet aerosol particle (n_{eff}), modified by the increased size is approximated by the volume-weighted average of the refractive indices of the dry aerosol substance (n_o) and the water (n_w) as

$$n_{\text{eff}} = n_w + (n_o - n_w) \left[\frac{r_o}{r(a_w)} \right]^3. \quad (12)$$

From these formulas, we note that the magnitude of the particle growth and the change of the refractive index with increasing RH depends on the size r_o of the dry aerosol. Also, the magnitude of the particle growth and the change of the refractive index with increasing RH (and therefore total PWV) depends on the aerosol type, because the water uptake [the ratio $m_w(a_w)/m_o$ in Eq. (10)] depends on the aerosol type.^{16–19} The relationship between the equivalent radius (r) and the relative humidity (RH) at different values of the equivalent radius r_o in the dry state has been computed for different models by Hanel.¹⁶ In particular, for values of RH ($<99\%$), the values of the ratio r/r_o are reasonably independent of r_o , and the smaller the value of the dry state equivalent radius r_o the larger the ratio r/r_o . In Fig. 10, we plot the surface level RH measurements from our rooftop weather station¹² for 23 February 2005. The RH for the morning was $\sim 70\%$, while by afternoon it had decreased to 30% . Figure 11 shows results obtained from the aerosol hydration model¹⁶ from which it can be seen that the observed change in the RH leads to an estimated change in the radius ratio of 20% . This modification can significantly change the refractive index in accordance with Eq. (12) and modify the resulting optical depth.

To see if the asymmetry observed in the SNR improvement factor can be attributed to the changes in aerosol properties due to hydration, we first modeled the dry aerosol seen in the afternoon as an urban accumulation mode that takes the form of a lognormal distribution with parameter values $r_m = 0.15 \mu\text{m}$, the dimensionless geometric standard deviation (GSD) parameter = 1.2, and complex refractive index $n = 1.5 - 0.2i$.²⁰ The total column number density of the

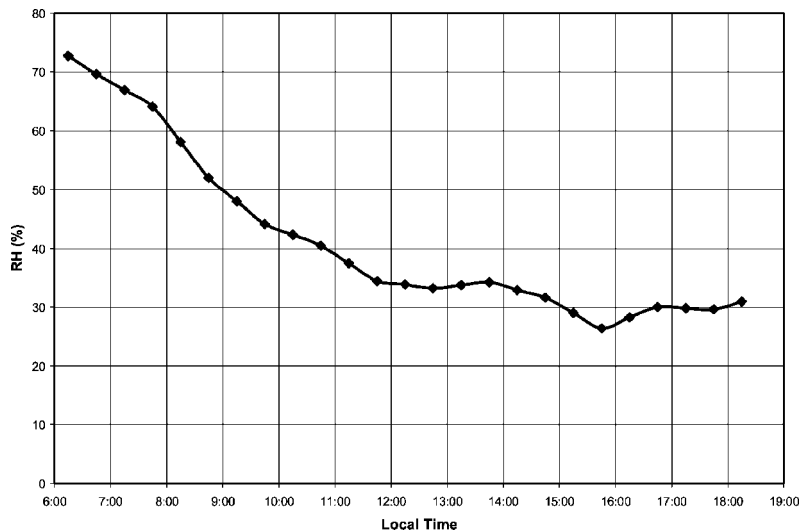


Fig. 10. RH versus local New York City time on 23 February 2005.

aerosol was then fixed using the afternoon column AOD = 0.09 reading obtained from the shadow-band radiometer. The effects of hydration were then modeled by continually sweeping the hydrated aerosol radius and calculating the resultant refractive index from Eq. (12) until the resultant AOD matched the measured morning value of $\tau_{\text{aer}} = 0.16$. The results are plotted in Fig. 12, and show that to match the $\tau_{\text{aer}} = 0.16$, the final effective radius is given by $r(a_w) = 0.18 \mu\text{m}$, which is consistent with the 20% increase in aerosol radius attributed to the RH changes.

Once the microphysical properties were estimated, we again utilize the single-scattering analysis to estimate the SNR improvement. Comparisons between measurements and theoretical results for the single-scattering model for these microphysical properties are given in Fig. 13. We see that reasonable agreement is obtained between this simplified theoretical approach and the experimental observations.

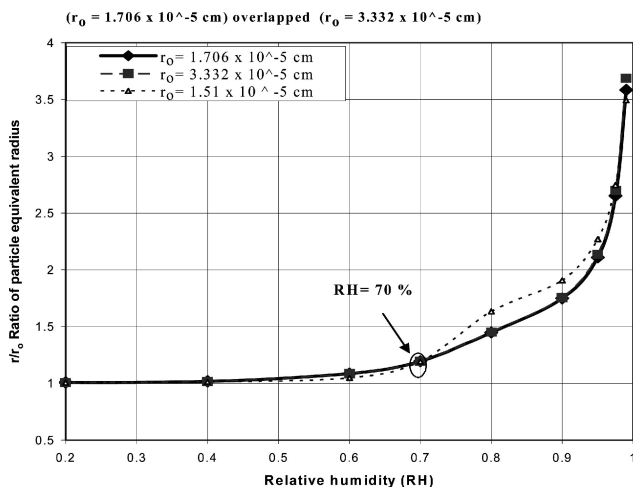


Fig. 11. Particle equivalent radius ratio r/r_0 versus RH at different equivalent radius r_0 in the dry state (RH = 0) and for two aerosol models at 20 °C temperature (Ref. 19).

6. Signal-to-Noise Ratio Improvement Azimuthal Dependence

Within the single-scattering theory, the polarization orientation at which the minimum P_b occurs should equal the azimuth angle of the Sun (see Fig. 1). To validate this result, the polarizer rotation angle was tracked (by rotating the detector analyzer) over several seasons since February 2004 and compared with the azimuth angle calculated using the U.S. Naval Observatory standard solar position calculator²¹ (14 April 2005). As expected, the polarizer rotation angle needed to achieve a minimum P_b closely tracks the azimuth angle, Fig. 14. This relationship is important, since it allows us to conceive of an automated approach that makes use of a precalculated solar azimuth angle as a function of time and date to automatically rotate and set both the transmitted lidar polarization and the detector polarizer at the orientations needed to minimize P_b . With an appropriate control system, it would then be possible to track the minimum P_b by rotating the detector analyzer and the transmission polarizer simultaneously to maximize the SNR, achieving the same results as would be done manually as described above. Plans are underway to integrate this automated approach into our

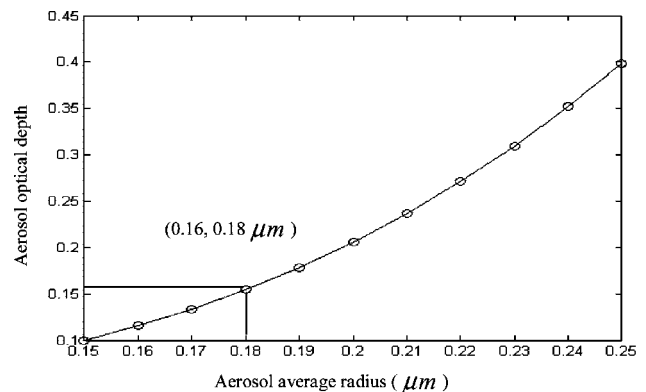


Fig. 12. Theoretical model, 23 February 2005.

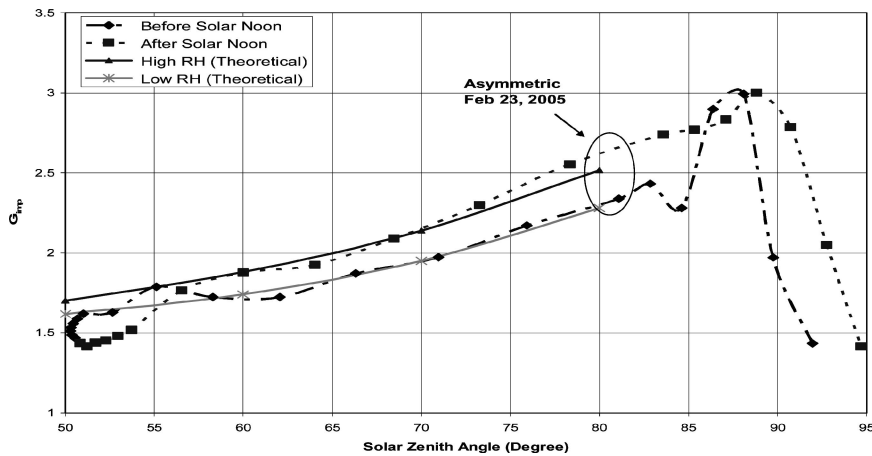


Fig. 13. Theoretical model agrees with experimental measurements, 23 February 2005.

lidar system. It is also useful to examine the potential impact of the polarization discrimination scheme on nonvertically pointing lidars. Typically, scanning lidars operating in an elastic or Raman backscatter mode, and are used to scan for particulates or trace constituents in the troposphere. They are of particular interest to air-quality monitoring applications where it is often desired to obtain information on spatial distributions of particulates and trace constituents above an urban area. This would include horizontal and near horizontal scans, along urban canyons, for example. Eye safety concerns severely limit acceptable visible lidar pulse energies for these applications, so any schemes to improve received SNRs are important. As seen earlier, for a vertically pointing lidar, the SNR improvement is greatest when the Sun's elevation is low, which restricts the period of large improvement to relatively short times in the early morning and late afternoon. The situation is quite different for a nonvertical scanning lidar. To illustrate, we consider a scanning lidar located at CCNY that is designed to scan the atmosphere above the downtown New York metropolitan skyline. Since CCNY is approximately 5 km north of the downtown area, the lidar azimuth angle does not need to vary

appreciably ($\pm 15^\circ$), and the lidar zenith angle need only vary from $50^\circ \leq \theta_{\text{lid}} \leq 80^\circ$ corresponding to relatively complete coverage through the planetary boundary layer.

From the vertical lidar results, Fig. 13, we note that significant SNR improvement (greater than a factor of 2) only occurs for scattering angles θ_{sc} above 70° . This result, when applied to the scanning geometry and making use of the symmetry of the scattering phase function, shows that significant SNR improvement will occur in the interval $70 < \theta_{\text{sc}} < 110$. To illustrate the differences between the vertical and the scanning case, we plot in Fig. 15, the variation in scattering angle for both the scanning and the vertical configurations for 21 June, a typically important time of the year for lidar measurements because of the increase in aerosol particulates in the summer months. The scattering angle and the complete solar positions (zenith and azimuth) needed to obtain it were again calculated using the solar position calculator.²¹ Figure 15 shows that for a good portion of the day (10:00 a.m.–2:00 p.m.), the scattering angle will lie in the range $70 < \theta_{\text{sc}} < 110$ permitting significant SNR improvement to be obtained by polarization discrimination. This is in contrast to the situation for a

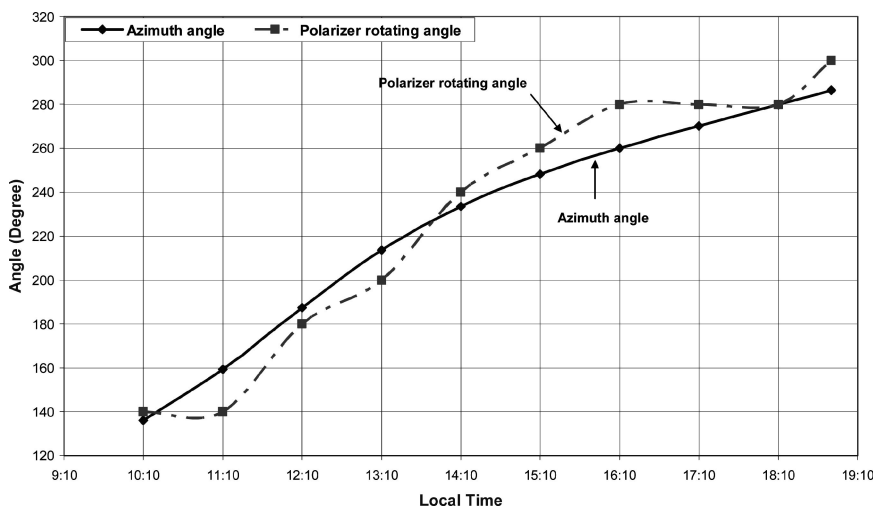


Fig. 14. Comparison of the solar azimuth angle and the angle of polarization rotation needed to achieve minimum P_b , 14 April 2005.

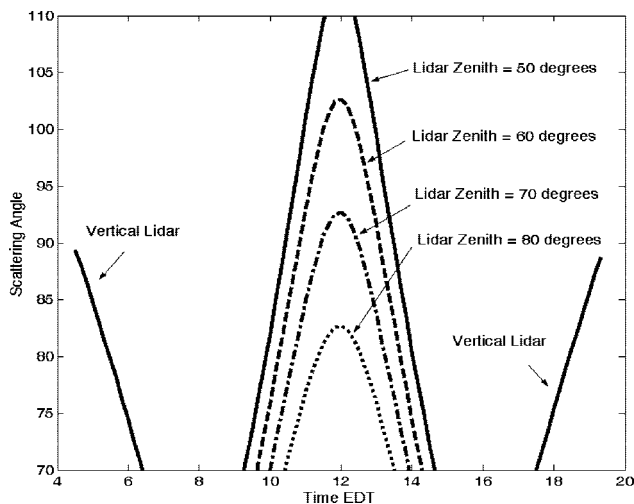


Fig. 15. Scattering angle θ_{sc} between the solar and the lidar directions for the scanning lidar geometry as a function of the lidar zenith angle and the time of day showing periods where SNR improvement can be significant. The vertical lidar result is also plotted to contrast to the time periods.

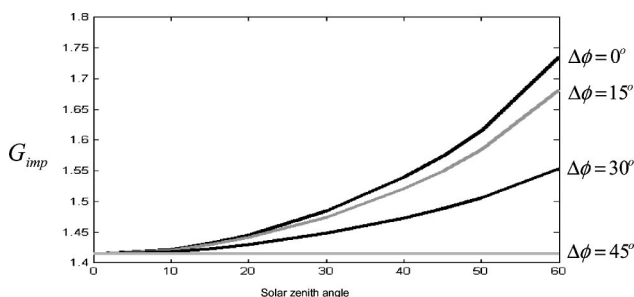


Fig. 16. Multiple-scattering model $\tau_{aer} = 0.5$ showing the minimum noise is parallel to the scattering plane regardless of optical depth. $\Delta\phi$ is the azimuth angle difference between the scattering and the polarization planes.

vertically pointing lidar where these improvements occur for very limited times near sunrise and sunset.

We have also examined, in a preliminary manner, the impact of multiple scattering on the polarization discrimination technique. While it is intuitive that the maximum noise suppression should occur when the receiver polarization is parallel to the scattering plane in the single-scattering regime, it is not so clear that this will hold for multiple scattering. However, it can be seen in Fig. 16 that even for high optical depth (multiple-scattering regime $\tau_{aer} = 0.5$), the maximum noise improvement factor calculated using a full polarized radiative transfer code developed at the NASA Goddard Institute for Space Science²² occurs when the differential azimuth angle is zero (i.e., the scattering plane and the observation plane are the same). Note also that when there is a 45° difference between the planes, only the minimum improvement of $\sqrt{2}$ is obtained since both polarization components are equal, and the background noise is effectively unpolarized.

7. Conclusions and Summary

SNR improvements obtained from lidar backscatter measurements, using the polarization selection-tracking scheme to reduce the sky background component, can significantly increase the far-range SNR as compared to unpolarized detection. This is equivalent to improvements in the effective lidar range of over 30% for a SNR threshold of 10. The improvement is largest for large scattering angles that, for vertical pointing lidars, occur near sunrise and/or sunset. It was also demonstrated that when the technique is applied to lidars scanning below 50° zenith angle, the time period under which significant SNR improvement can occur extends over a significant portion of the midday (10 a.m.–2 p.m.) thereby extending the utility of the technique. A theoretical model that simulates the background skylight within the single-scattering approximation was developed and showed fairly accurate predictions of the SNR improvement factor. Asymmetric skylight reduction was sometimes observed in experimental results and is explained by the measured increase in PWV and subsequent modification of aerosol optical depth by dehydration from morning to afternoon. Finally, since the polarization axis follows the solar azimuth angle even for high aerosol loading as demonstrated using radiative transfer simulations, it is quite conceivable to automate this procedure simply by using solar position calculators to orient the polarization axes.

In all previous discussions, clear sky conditions were assumed. The impact of clouds in the lidar field of view is more complex. From intuitive considerations, it can be conjectured that on a partially sunny day, a lidar viewing directly scattered sunlight from a cloud, with large single-scattering components, will see a significant polarized light component in the detected radiation. Under those circumstances, which apply primarily to the scanning lidar orientations, polarization discrimination should improve the SNR. However, in other circumstances such as a complete overcast sky, the background is dominated by multiple-scattered light, which is depolarized so the technique is probably much less useful. Clearly, more detailed examinations are needed to quantify the effects of multiple scattering by both dry and hydrated aerosols as well as clouds.

This work was partially supported under contracts from NOAA NA17AE1625 and NASA NCC-1-03009.

References

1. R. M. Schotland, K. Sassen, and R. J. Stone, "Observations by lidar of linear depolarization ratios by hydrometeors," *J. Appl. Meteorol.* **10**, 1011–1017 (1971).
2. K. Sassen, "Depolarization of laser light backscattered by artificial clouds," *J. Appl. Meteorol.* **13**, 923–933 (1974).
3. C. M. R. Platt, "Lidar observation of a mixed-phase altostratus cloud," *J. Appl. Meteorol.* **16**, 339–345 (1977).
4. K. Sassen, "Scattering of polarized laser light by water droplet, mixed-phase and ice crystal clouds. 2. Angular depolarization and multiple scatter behavior," *J. Atmos. Sci.* **36**, 852–861 (1979).
5. C. M. R. Platt, "Transmission and reflectivity of ice clouds by

- active probing,” in *Clouds, Their Formation, Optical Properties, and Effects*, P. V. Hobbs, ed. (Academic, 1981), pp. 407–436.
6. D. S. Kokkinos and S. A. Ahmed, “Atmospheric depolarization of lidar backscatter signals,” in *Lasers '88: Proceedings of the International Conference, Lake Tahoe, Nevada*, Paper No. A90-30956 12-36. (STS Press, McLean, Virginia, 1989), pp. 538–545.
 7. G. P. Gobbi, “Polarization lidar returns from aerosols and thin clouds: a framework for the analysis,” *Appl. Opt.* **37**, 5505–5508 (1998).
 8. N. Roy, G. Roy, L. R. Bissonnette, and J. Simard, “Measurement of the azimuthal dependence of cross-polarized lidar returns and its relation to optical depth,” *Appl. Opt.* **43**, 2777–2785 (2004).
 9. J. Hansen and L. Travis, “Light scattering in planetary atmospheres,” *Space Sci. Rev.* **16**, 527–610 (1974).
 10. Y. Y. Hassebo, B. Gross, F. Moshary, Y. Zhao, and S. Ahmed, “Polarization discrimination technique to maximize lidar signal-to-noise ratio,” in *Polarization Science and Remote Sensing II*, J. A. Shaw and J. S. Tyo, eds., *Proc. SPIE* **5888**, 93–101 (2005).
 11. Y. Y. Hassebo, B. M. Gross, M. M. Oo, F. Moshary, and S. A. Ahmed, “Impact on lidar system parameters of polarization selection/tracking scheme to reduce daylight noise,” in *Lidar Technologies, Techniques, and Measurements for Atmospheric Remote Sensing*, U. N. Singh, ed., *Proc. SPIE* **5984**, 53–64 (2005).
 12. NOAA-CREST, <http://www.fsl.noaa.gov>.
 13. M. V. Klein, *Optics* (Wiley, 1970).
 14. R. M. Measures, *Laser Remote Sensing* (Wiley, 1984).
 15. K. N. Liou, *An Introduction to Atmospheric Radiation* (Academic, 2002).
 16. G. Hanel, “The properties of atmospheric aerosol particles as functions of the relative humidity at thermodynamic equilibrium with the surrounding moist air,” in *Advances in Geophysics*, H. E. Landsberg and J. Van Mieghem, eds. (Academic, 1976), Vol. 19, pp. 73–188.
 17. P. V. N. Nair and K. G. Vohra, “Growth of aqueous sulfuric acid droplets as function of relative humidity,” *J. Aerosol Sci.* **6**, 265–271 (1975).
 18. G. Hanel and M. Lehmann, “Equilibrium size of aerosol particles and relative humidity: new experimental data from various aerosol types and their treatment for cloud physics application,” *Contrib. Atmos. Phys.* **54**, 57–71 (1981).
 19. B. Yan, K. Stamnes, W. Li, B. Chen, J. J. Stamnes, and S.-C. Tsay, “Pitfalls in atmospheric correction of ocean color imagery: how should aerosol optical properties be computed?” *Appl. Opt.* **41**, 412–423 (2002).
 20. E. P. Shettle and R. W. Fenn, *Models of the Aerosols of the Lower Atmosphere and the Effects of Humidity Variations on Their Optical Properties*, Project 7670 (Air Force Geophysics Laboratory, Massachusetts, 1979).
 21. U.S. Naval Observatory Astronomical Applications, <http://aa.usno.navy.mil/data/docs/AltAz.html>.
 22. J. Chowdhary, B. Cairns, and L. D. Travis, “The contribution of the water leaving radiances to multiangle, multispectral polarimetric observations over the open ocean: bio-optical model results for Case I waters,” special issue, “Polarization imaging and remote sensing,” *Appl. Opt.* **45**, 5542–5567 (2006).